Journal of
Manufacturing and Materials Processing

MDPI

Article

Temperature Evaluation of Cladding Beads and the Surrounding Area during the Laser Metal Deposition Process

Yorihiro Yamashita [1,*], Kholqillah Ardhian Ilman [2,3], Takahiro Kunimine [4] and Yuji Sato [5]

[1] Department of Mechanical Engineering, National Institute of Technology, Ishikawa College, Kitachujo, Tsubata 929-0392, Ishikawa, Japan
[2] Division of Mechanical Science and Engineering, Graduate School of Natural Science and Technology, Kanazawa University, Kakuma-machi, Kanazawa 920-1192, Ishikawa, Japan; kholqillah@stu.kanazawa-u.ac.jp
[3] Department of Mechanical Engineering, Faculty of Engineering, Universitas Muhammadiyah Surakarta, Sukoharjo 57169, Central Java, Indonesia
[4] Faculty of Mechanical Engineering, Institute of Science and Engineering, Kanazawa University, Kakuma-machi, Kanazawa 920-1192, Ishikawa, Japan; kunimine@se.kanazawa-u.ac.jp
[5] Department of Laser Materials Processing, Research Division of Materials Joining Process, Joining & Welding Research Institute, Osaka University, Mihogaoka 11-1, Ibaraki 567-0047, Osaka, Japan; sato.yuji.jwri@osaka-u.ac.jp
* Correspondence: y.yamashita@ishikawa-nct.ac.jp; Tel.: +81-76-288-8099

Abstract: Cracks usually generate during the formation of beads composed of a WC-12mass%Co cemented carbide by the laser metal deposition (LMD). Measuring temperatures of the formed bead and substrate during the LMD process is important for realizing crack-free beads. In this study, temperatures of the substrate around the formed bead during the LMD process were measured using a thermoviewer. Temperatures of the formed beads during the LMD process were predicted by simulation based on the thermal conduction analysis using the experimentally measured temperatures of the substrate. The experimental results obtained during forming the WC-12mass%Co cemented carbide beads on JIS SKH51 (ISO HS-6-5-2) substrates showed that the maximal temperatures of the substrates at 0.2 mm away from the center of the formed beads ranged from 229 °C to 341 °C at laser powers ranging from 80 W to 160 W. The predicted maximal temperatures of the formed beads were in the range of 2433 °C to 4491 °C in the simulation using a laser absorption coefficient of 0.35 for the substrate. Validity of these simulation results was discussed based on the melting point of the substrate and microstructures of the formed WC-12mass%Co cemented carbide beads.

Keywords: laser metal deposition (LMD); multi beam laser; cemented carbide; thermoviewer; thermal conduction analysis

Citation: Yamashita, Y.; Ilman, K.A.; Kunimine, T.; Sato, Y. Temperature Evaluation of Cladding Beads and the Surrounding Area during the Laser Metal Deposition Process. *J. Manuf. Mater. Process.* **2023**, *7*, 192. https://doi.org/10.3390/jmmp7060192

Academic Editors: Mohsen K. Keshavarz and Esmaeil Sadeghi

Received: 19 August 2023
Revised: 17 October 2023
Accepted: 20 October 2023
Published: 28 October 2023

1. Introduction

In recent years, industrial sectors have witnessed a dramatic increase in the demand for inexpensive jigs with superior mechanical properties. Nonetheless, the conventional choice of using cemented carbides to meet these requirements has presented two significant hurdles. First, cemented carbides are expensive materials, which make it difficult to manufacture cost-effective jigs [1]. Second, when costs become the primary concern, the mechanical properties of cemented carbides tend to deteriorate [2]. Utilizing a tool steel for a majority of jig components has emerged as a promising strategy to address these issues. Tool steel is a less expensive alternative material that offers decent mechanical properties [3]. By employing tool steels in the majority of the jig's components, manufacturers can reduce the overall price without sacrificing performance. In order to ensure that the jigs possess sufficient wear resistance, cemented carbides are applied selectively to specific regions that experience excessive wear [4]. This strategic placement of cemented carbides enables the instruments to maintain their durability and performance in critical areas while minimizing the associated cost. Additive manufacturing (AM) technologies are promising approaches

to promote this strategic placement of cemented carbides. AM technologies are already being used for industrial products in the fields of the aerospace industry, biomedical applications, and so on [5–9].

Among AM technologies, the laser metal deposition (LMD) method is an innovative process that implements a laser as a precise and controlled heat source to melt powder materials and generate a cladding layer with a distinct composition on the substrate [10–15]. This method minimizes the thermal impact on the substrate and facilitates the formation of a specific localized cladding layer. It can also enable the formation of a cladding layer with a specific composition tailored to the desired properties or functionalities [16]. Different types of powder materials can be fed into the laser beam, ranging from metals and alloys to ceramics or composite powders [17]. This flexibility enables the production of cladding layers with superior hardness, wear resistance, corrosion resistance, or even entirely new material combinations [18]. Nevertheless, one of the problems associated with this method is its tendency to frequently generate voids and cracks within the deposited spots, which, in turn, can undermine its structural integrity and strength [19,20]. Consequently, it has become imperative to conduct research and experiments aiming to develop and implement effective techniques to mitigate and reduce the occurrence of these undesirable voids and cracks. By doing so, it becomes possible to enhance the practical viability and reliability of this method for a wide range of real-world applications.

One of the reasons for the formation of voids is that granulated powders of cemented carbides include many voids. In order to reduce the voids, plasma treatment has been applied to granulated powders [21]. Suppressing cracks is also important for successful LMD processing. Extensive research has shown that a direct relationship exists between the laser input energy and the number of the formed cracks, as well as the size of the cracks, during the LMD process [19]. By accurately measuring temperatures of the formed bead and its immediate surroundings, we can obtain valuable insights into the thermal dynamics that lead to forming cracks. Crack initiation can be attributed to differences in material properties between a substrate and a cladding material, as well as changes in microstructures. Temperature is a key factor to understand these phenomena in detail [22]. Many researchers have attempted to measure temperatures of cladding beads using a two-color radiation thermometer, but it is assumed that the values of the emissivity for the radiation with the respective two wavelengths are constant and the temperature is accurate. However, it is difficult to measure the temperature accurately because the values of the emissivity for the radiation with the two respective wavelengths must be constant. Therefore, in this study, a blackbody coating material with a specified emissivity was applied on substrates. Then, substrate temperatures were accurately measured. Based on the results, temperatures of the cladding beads were estimated by simulation because the temperatures of the beads cannot be measured directly due to the melting of the blackbody-coated substrates. The estimated temperatures of the cladding beads are important information to consider the changes in metallographic microstructures that lead to crack initiation and propagation. It is expected that this approach promotes the development of LMD technology with respect to crack suppression.

2. Experimental Procedures

2.1. Laser Metal Deposition

The LMD method is a technology that can form a metallic layer on the surface of a substrate by melting a supplied metallic powder using a laser beam. In this study, a multi-beam-type LMD (M-LMD) device (ALPION Series, Muratani Machine Inc., Ishikawa, Japan) was used [23]. The M-LMD device has been developed for realizing the precise and minimized heat-affected zones. In the M-LMD device, multiple laser beams are focused on an area of the surface of the substrate to form a cladding layer. The schematic diagram of this device is shown in Figure 1.

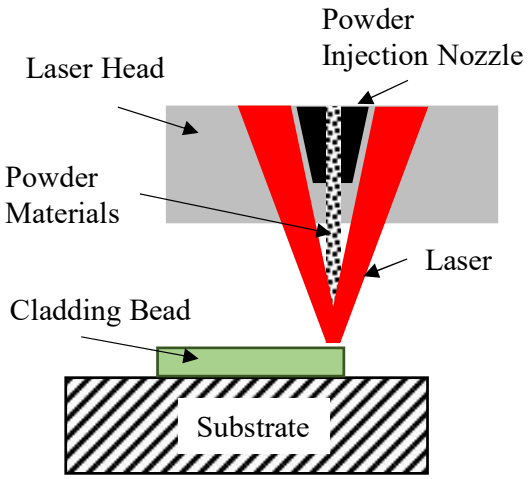

Figure 1. Schematic diagram of the M-LMD device.

Table 1 presents the parameters for forming beads using the M-LMD device applied in this study. With this M-LMD device, the wavelength of the six diode laser beams is 975 nm. The laser-focusing spot diameter was 0.3 mm. The scanning speed was maintained at 20 mm/s, and five conditions of laser power were set at 80, 100, 120, 140, and 160 W (in 20 W increments). The used substrate was JIS SKH51 (ISO HS-6-5-2) with dimensions of 20 mm × 40 mm × 60 mm. The used powder was a WC-12mass%Co cemented carbide (Powlex Co., LTD., Tokyo, Japan). The powder was supplied at 20 mg/s with argon gas. A bead with a length of 10 mm was formed by the M-LMD device. The position for forming beads on the substrate is shown in Figure 2. The beads were formed at a position of 5 mm away from the left edge of the substrate and moved 10 mm to the right. Forming a bead was performed three times in each condition.

Table 1. Parameters for forming beads using the M-LMD.

Parameter	Unit	Value				
Laser power	W	80	100	120	140	160
Scanning speed	mm/s	20				
Powder feeding rate	mg/s	20				
Laser wavelength	nm	975				
Laser focusing spot diameter	mm	0.3				

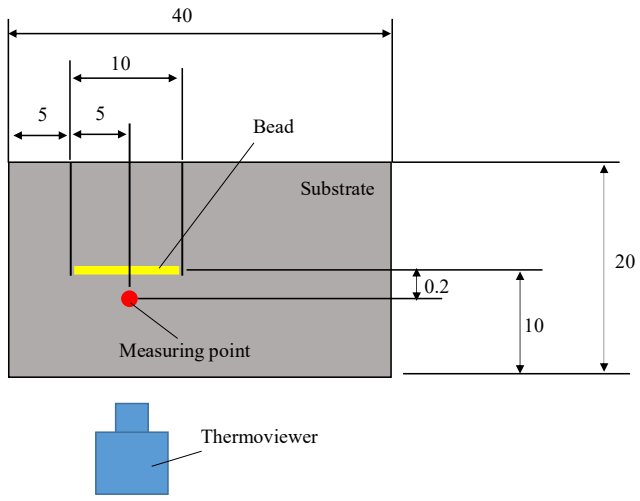

Figure 2. Schematic diagram showing the position of the bead on the substrate and the temperature measurement position using a thermoviewer.

2.2. Temperature Measurement by Thermoviewer

Temperature measurements were conducted using a thermoviewer (PI 640MO, Optris). The specification of the thermoviewer device is listed in Table 2. When utilizing the thermoviewer for temperature monitoring during the M-LMD process, it is essential to precisely determine the emissivity of the used materials. Therefore, the substrate is in a molten state in the laser-irradiated region, making it difficult to determine the emissivity. In order to overcome this problem and guarantee accurate temperature measurements, a blackbody coating material (JSC-3, Japansensor Inc., Tokyo, Japan) was carefully coated onto the surface of the substrates before performing the M-LMD process. The blackbody coating material exhibited distinct characteristics that provide it well-suited for this particular application. With a remarkable thermal stability reaching a temperature as high as 1500 °C, this coating material exhibits an exceptional capacity to endure the rigorous thermal conditions encountered throughout the LMD process. Moreover, it is worth noting that the blackbody coating material exhibits a well-established and consistent emissivity value of 0.94, thereby offering a dependable point of reference for accurate temperature examinations. Through the application of the blackbody coating material, the inherent uncertainties arising from the molten state of the substrate and the variations in emissivity within the surrounding areas are effectively alleviated. The implementation of this approach facilitates the acquisition of temperature measurements that exhibit enhanced precision and reliability throughout the M-LMD process. The implementation of the blackbody coating material guarantees the attainment of dependable temperature measurements, thereby enabling accurate control and observation of the M-LMD process.

Table 2. Specifications for the thermoviewer.

Specification Items	Unit	Value
Resolution	pixel	640 × 120
Sensitivity	K	0.075
Viewing angle	degree	12 × 9
Temperature range	°C	200~1500
Frame rate	Hz	125

In Figure 3, the experimental setup for temperature monitoring using the thermoviewer is shown. It demonstrates that a powder injection nozzle is fixed above the bead forming region, facilitating powder injection and laser irradiation. As a result, direct temperature measurement from above is not feasible due to the obstructed view caused by the presence of the nozzle. Moreover, employing the thermoviewer to determine the location of laser irradiation after taking temperature measurements may introduce inaccuracies due to the specific angle employed during the measurement process. To tackle this challenge and ensure accurate temperature measurements, a leveling device was employed, as depicted in Figure 4. The purpose of this leveling device is to determine the camera angle used for the temperature measurements. By precisely measuring the camera angle, any potential errors arising from the specific angle during the measurement process can be accounted for and mitigated. For the described experiment, the camera angle was measured to be 31° using the leveling device. This measurement serves as a crucial calibration parameter that enables the accurate interpretation of the temperature data obtained from the thermoviewer.

In order to conduct a comprehensive thermal analysis, temperature measurements were acquired at a specific point situated at a distance from the bead. The temperature measurements were graphically represented in order to observe and analyze the temporal variations in temperature. Despite the presence of a blackbody coating material on the surface of the substrate in the bead area, the cladding process was executed on the aforementioned blackbody coating material, leading to the emergence of diverse emissivity. Additionally, it is important to consider the pixel size and field of view of the thermoviewer utilized in this study. Each pixel of the thermoviewer corresponds to an area of 0.03125 mm × 0.03125 mm. With this information, the location for measuring the

temperature can be determined, taking into account the camera angle as well. Therefore, this study chose 0.2 mm away from the bead center as the optimal location for temperature evaluation, where the integrity of the blackbody coating material is not affected by the M-LMD process (in Figure 2).

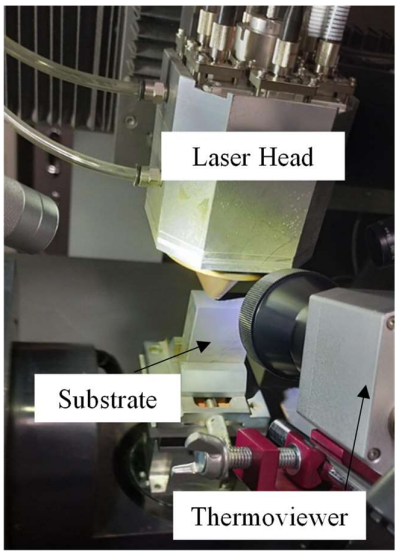

Figure 3. Experimental setup for temperature monitoring using the thermoviewer.

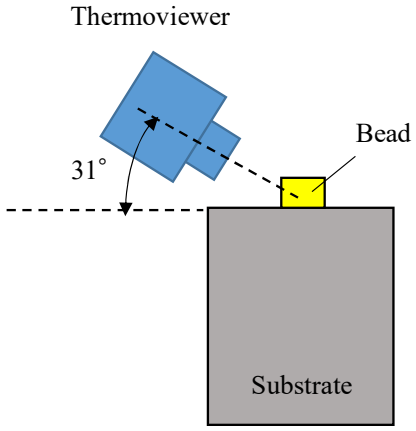

Figure 4. Camera angle relative to the bead position.

2.3. Temperature Estimation by Simulation

To supplement the experimental results, a simulation of the LMD process was performed using Simufact Welding, which is specialized thermal conduction analysis software. This simulation sought to predict the temperature distribution near the laser-irradiated area. In this simulation, we attempted to predict temperature distribution of the substrate at a distance from the laser irradiation position and the bead area. Simufact Welding software uses advanced algorithms and numerical methods to simulate the complex heat transfer phenomena that occur during the LMD process. By entering relevant information such as the laser power, scanning speed, material properties, and boundary conditions, the software can generate a temperature profile around the laser-irradiated area. In the simulation, heat energy was applied to the substrate and a bead part made by CAD data was prepared in advance. The CAD data were converted into mesh data for detailed analysis. Then, the temperature was calculated based on the heat conduction analysis.

Figure 5 illustrates the models used for the simulation of the substrate and the bead. The substrate was set to 20 mm × 40 mm × 1 mm. Normally, the thickness

dimension should match the actual substrate. However, no significant effect on the temperature of the substrate and the bead was observed when varying the thickness dimension. Therefore, for this study, the thickness was set to 1 mm. A mesh size of 0.43 mm × 0.43 mm × 0.1 mm was used for the substrate model. Additionally, for the area surrounding the bead region, considering a laser focal diameter of 0.3 mm, the mesh size was set to 0.05 mm × 0.05 mm × 0.1 mm. The material used for the substrate model was JIS SKH51. As depicted in Figure 5, the bead size was set to 10 mm × 0.3 mm × 0.1 mm. For the bead model, a mesh size of 0.05 mm × 0.05 mm × 0.05 mm was created. The material used for the bead was the WC-12mass%Co cemented carbide. The bead was placed in the center of the substrate. The physical properties of the JIS SKH51 and the WC-12mass%Co cemented carbide are presented in Table 3 [24–27]. The physical properties of the WC-12mass%Co cemented carbide were calculated from the physical properties of WC and Co obtained from [28].

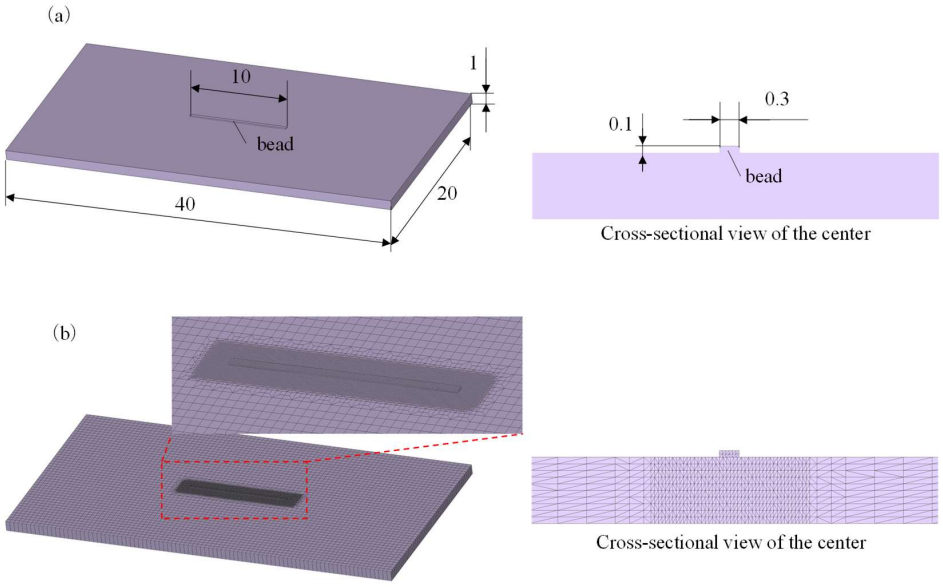

Figure 5. (**a**) CAD model and (**b**) meshes in the model for the simulation.

Table 3. Physical properties of the JIS SKH51, WC, Co, and WC-12mass%Co cemented carbide.

Properties	Unit	SKH51	WC	Co	WC-12mass%Co
Thermal conductivity	W/(m·K)	22	29.3	99.2	35.1
Specific heat capacity	J/(g·K)	0.52	0.18	0.42	0.20
Density	g/cm^3	8.2	15.8	8.9	14.5
Melting temperature	K	1703	3058	1767	2823
Latent heat for melting	J/kg	272,500	445,000	260,000	422,800

First, by assuming that density is linear with volume fraction, the density, ρ(g/cm^3), of the cemented carbide was calculated from the following equation:

$$\rho = \rho_m(1 - R) + \rho_b R, \quad (1)$$

where ρ_m is the density of WC (g/cm^3), ρ_b is the density of Co (g/cm^3), and R is the volume fraction of Co. Second, by assuming that specific heat capacity was linear with mass fraction, specific heat capacity, c (J/(g·K)), was calculated from the following equation:

$$c = c_m\left(1 - \frac{1}{1 + \left(\frac{1}{R} - 1\right)\frac{\rho_m}{\rho_b}}\right) + c_b\left(\frac{1}{1 + \left(\frac{1}{R} - 1\right)\frac{\rho_m}{\rho_b}}\right), \quad (2)$$

where c_m is the specific heat capacity of WC (J/(g·K)) and c_b is the specific heat capacity of Co (J/(g·K)). By assuming that latent heat for melting is linear with mass fraction, latent heat for melting, L (J/kg), was calculated from the following equation:

$$L = L_m\left(1-\frac{1}{1+\left(\frac{1}{R}-1\right)\frac{\rho_m}{\rho_b}}\right)+L_b\left(\frac{1}{1+\left(\frac{1}{R}-1\right)\frac{\rho_m}{\rho_b}}\right), \quad (3)$$

where L_m is latent heat for the melting of WC (J/kg) and L_b is latent heat for the melting of Co (J/kg). Finally, thermal conductivity, K (W/(m·K)), was calculated using a model based on the parallel and series composite springs described by the following equation:

$$K = K_m(1-\sqrt{R})+\left(\frac{1}{\frac{1-\sqrt{R}}{K_m}+\frac{\sqrt{R}}{K_b}}\right)\sqrt{R}, \quad (4)$$

where K_m is the thermal conductivity of WC (W/(m·K)) and K_b is the thermal conductivity of Co (W/(m·K)). The melting temperature, T (K), was determined from the pseudo-equilibrium phase diagram of WC-Co cemented carbides [29].

For temperature predictions through simulations, two points were considered: a point in the substrate away from the laser-irradiated area and another point at the center of the laser-irradiated area. The simulation parameters are presented in Table 4. The scanning speed was kept constant at 20 mm/s, and the laser power was varied in five conditions from 80 W to 160 W in increments of 20 W. The radius and depth of the heat source are illustrated in Figure 6. The cylindrical heat source radius, r (mm), was set at 0.15 mm, considering the laser-focusing spot diameter. The heat source depth, d (mm), was set at 0.1 mm, because a laser absorption phenomenon usually occurred on the surface of the substrate. The heat source position was set between the surface of the substrate and that of the bead in the simulation. The laser absorption coefficients of the powder (WC-12mass%Co) and the substrate (JIS SKH51), determined using a laser wavelength of 1 μm, were 0.82 [30] and 0.35 [31], respectively. Most of the laser passes through the powder and reaches the substrate; therefore, the energy efficiency of heat source was set at 0.35.

Table 4. Simulation parameters.

Parameter	Unit	Value				
Laser power	W	80	100	120	140	160
Scanning speed	mm/s			20		
Cylindrical heat source radius, r	mm			0.15		
Cylindrical heat source depth, d	mm			0.1		

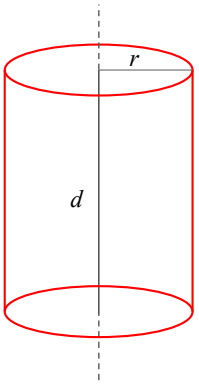

Figure 6. The cylindrical heat source with a radius, r, and a depth, d.

3. Results and Discussion

3.1. Temperature around the Bead Measured by the Thermoviewer

Figure 7 presents thermal profiles during the experiments. The temperature changes over time for each laser condition are shown in Figure 8. It can be observed that as the laser power increases, the maximal temperature of the substrate also increases. Additionally, Figure 9 shows a bar graph of the maximal temperature for each laser condition. It can be observed that the temperature reached 229 °C for a laser power of 80 W and 341 °C for a laser power of 160 W. These findings can be explained using the equation for the input energy per unit area, E (J/mm^2), as follows:

$$E = \frac{P}{VD}, \tag{5}$$

where P is the laser power (W), V is the laser scanning speed (mm/s), and D is the laser spot diameter (mm).

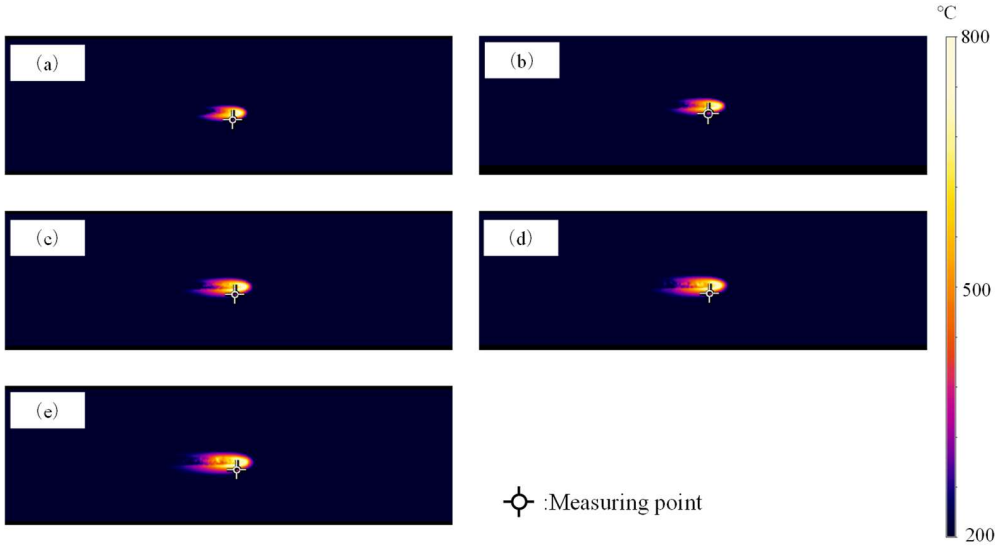

Figure 7. Thermal distributions during the experiments at (**a**) 80 W, (**b**) 100 W, (**c**) 120 W, (**d**) 140 W, and (**e**) 160 W.

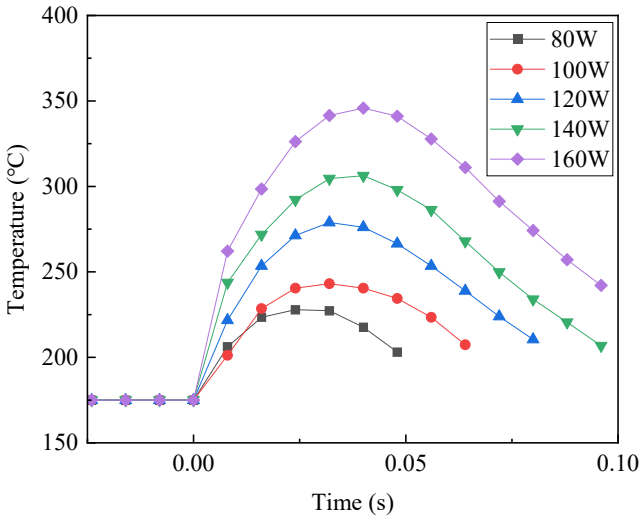

Figure 8. Profiles of substrate temperature obtained at a point of 0.2 mm away from the bead center using the thermoviewer for each laser condition.

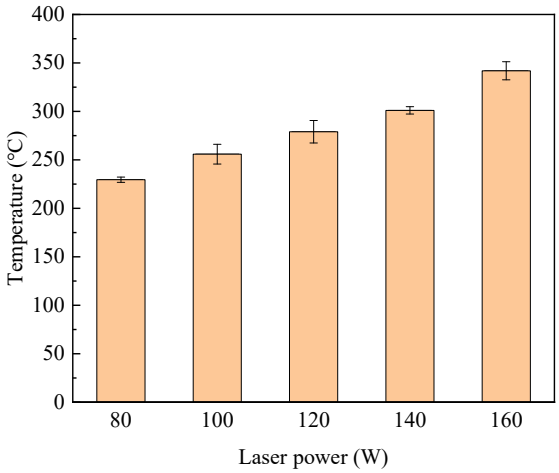

Figure 9. Maximal temperatures of the substrates obtained via the thermoviewer.

In this experiment, the laser scanning speed was maintained at a constant value for each condition, while the laser power was varied. As a result, the input energy to the substrate was directly influenced by the laser power. When the laser power increased, it led to a corresponding increase in the input energy delivered to the substrate. As the input energy increased, more heat was generated, resulting in a higher peak temperature within the substrate. Therefore, it can be inferred that the increase in laser power is the primary factor contributing to the elevation of the peak temperature in the substrate.

3.2. Temperature Prediction by the Simulation

Figure 10 shows the simulation images corresponding to each LMD condition. The images reveal notable changes, i.e., the thermal influence on the substrate expanded as the laser power increased. This expansion of thermal influence signifies that a higher laser power resulted in a larger affected area on the substrate due to the increased heat input.

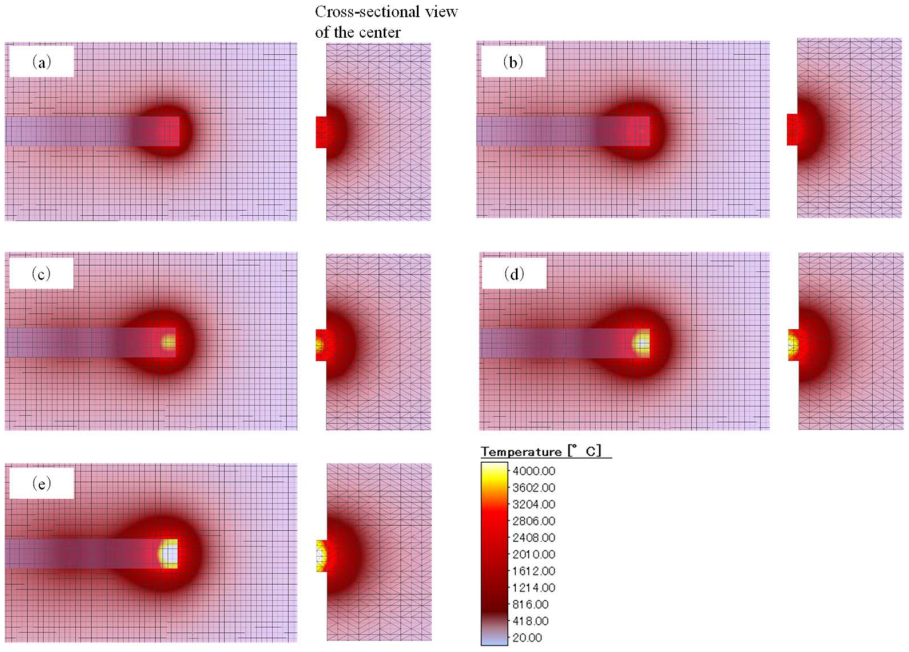

Figure 10. Temperature distribution of the beads, substrate surface, and cross-section at the center of the substrate corresponding to each LMD condition obtained by the simulation with the laser absorption coefficient of 0.35 after 0.25 s from the start of forming the bead. (**a**) 80 W, (**b**) 100 W, (**c**) 120 W, (**d**) 140 W, and (**e**) 160 W.

Figure 11 shows the simulated maximum temperatures at a position 0.2 mm from the center of the bead area, which is the same position as in the thermoviewer experiment. The simulation was performed using a laser absorption coefficient of 0.35, which was the absorption coefficient of the substrate. In addition, temperature simulation results obtained using the laser absorption coefficient of 0.1 and 0.2 are shown. At a laser absorption coefficient of 0.35, the simulated maximum temperatures did not match the experimental results obtained by the thermoviewer. At the laser absorption coefficient of 0.1, the temperature-incremental trend was close to the experimental results obtained via the thermoviewer. Figure 12 shows the maximal temperatures at the center of the beads and a height of 0.05 mm from the substrate surface for each laser irradiation condition. When a laser absorption coefficient of 0.1 was applied, the maximal temperature was 1465 °C even at 160 W. This means that the maximal temperature of the bead formed by 160 W was barely able to reach the melting point of the substrate. Thus, it can be said that applying the laser absorption coefficient of 0.1 is not appropriate for forming beads. Considering the situation in which the bead was formed at 80 W, it is reasonable that the absorption coefficient should be 0.2 or higher. However, these values of absorption coefficient do not match the temperature measurement results with the thermoviewer, as shown in Figures 9 and 11. Gas blowing, which was used when supplying the powder during the LMD process, was not taken into account in the simulation; thus, it can be considered that the simulation condition without gas blowing caused the higher temperature at the surface of the substrate. Figure 13a–c show SEM images of the cross-sections of the beads. At a laser power of 80 W, angular grains of the WC phase and dendritic structures composed of M_6C phase [15] can be seen as shown in Figure 13a. With the increase in laser power, the volume fraction of the WC grains decreased. Instead, it can be confirmed that the grain growth of the dendritic structures of M_6C phase progressed as the laser output increased. Considering the formed microstructures and the pseudo-equilibrium phase diagram [29], it was suggested that simulation using a laser absorption coefficient between 0.1 and 0.2 may indicate more accurate temperatures of the beads in terms of microstructural point of view. The M_6C phase is well known for affecting the fracture toughness [32]. As the laser power increased, the volume fraction and size of M_6C phase increased. These microstructural changes can be considered as a contributing factor for the increase in the number of cracks. In our previous research, we investigated the number of cracks using an AE sensor and obtained the results shown in Figure 14 [18]. These results show that the number of cracks indeed increased as the laser power increased, resulting in increasing the risk of crack initiation. These results correspond well with the microstructural observations of the formed beads.

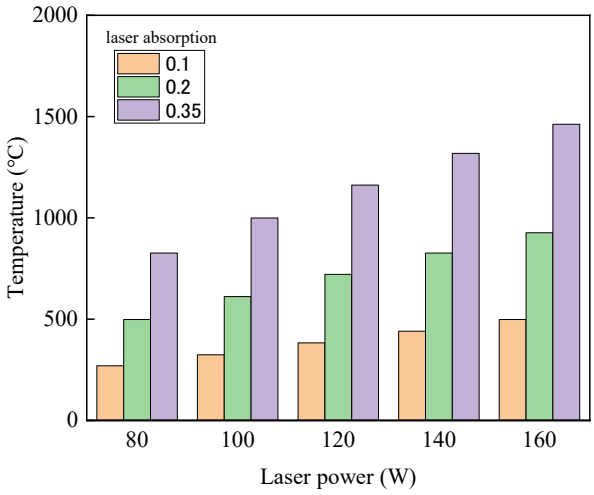

Figure 11. Maximal temperatures at 0.2 mm away from the bead area for each laser power using the simulation approach.

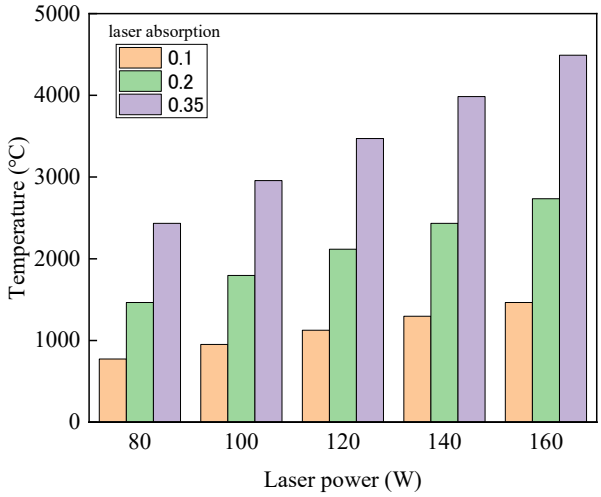

Figure 12. Maximal temperatures at the center of the beads for each laser power using the simulation approach.

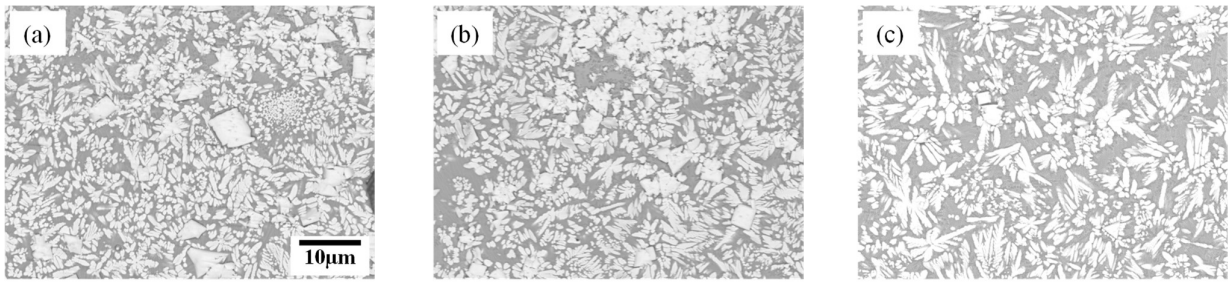

Figure 13. Cross-sectional SEM images of the beads cladded on the substrates with (**a**) 80 W, (**b**) 120 W, and (**c**) 160 W.

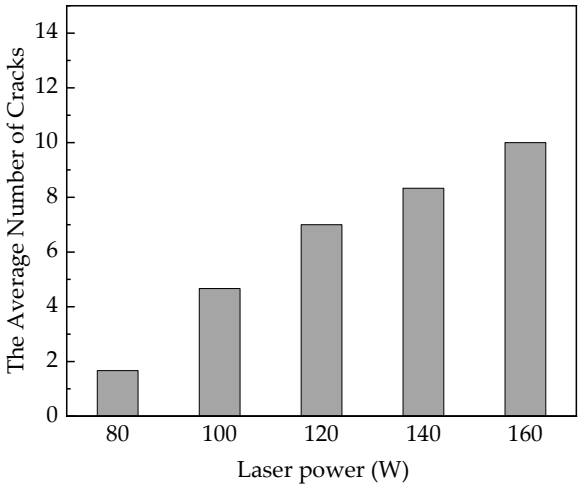

Figure 14. The average number of cracks detected by the AE sensor vs. laser power [18].

4. Conclusions

The substrate temperatures around the beads were measured using the thermoviewer when the beads were formed by M-LMD (multi-beam-type laser metal deposition). The internal temperatures of the beads during the LMD process were evaluated through the simulation based on the temperature measurements of substrates obtained using the thermoviewer. The obtained results are summarized below.

(1) An increase in laser power leads to an increase in substrate temperature. The substrate temperatures at a point located 0.2 mm away from the center of the bead area, with a scanning speed of 20 mm/s and laser powers of 80 W and 160 W, were found to be 229 °C and 341 °C, respectively.
(2) Based on the simulation results obtained using the thermal conduction analysis software, at a laser absorption coefficient of 0.35, temperatures of the bead area were predicted to be approximately 2433 °C at a laser power of 80 W and 4491 °C at a laser power of 160 W, at a scanning speed of 20 mm/s. However, the simulated maximum temperatures at a position of 0.2 mm from the center of the bead area using the laser absorption coefficient of 0.35 did not match the experimental results obtained by thermoviewer. Considering the melting point of substrate and formed microstructures of the beads, it was suggested that the simulation results using laser absorption coefficients between 0.1 and 0.2 may indicate more accurate temperatures of the beads.
(3) At a laser power of 80 W, angular grains of WC phase and dendritic structures composed of M_6C phase were observed in the formed bead. With the increase in laser power, the volume fraction of the WC grains decreased. In addition, it can be confirmed that the grain growth of the dendritic structures of M_6C phase progressed as the laser output increased.

Author Contributions: Conceptualization, Y.Y., T.K. and Y.S.; methodology, Y.S. and Y.Y.; software, K.A.I. and Y.Y.; validation, Y.Y. and T.K.; formal analysis, Y.Y. and K.A.I.; investigation, Y.Y., K.A.I., Y.S. and T.K.; resources, Y.Y. and T.K.; writing—original draft preparation, Y.Y. and K.A.I.; writing—review and editing, T.K. and Y.S. All authors have read and agreed to the published version of the manuscript.

Funding: This study was supported by JSPS KAKENHI Grant Number JP22K03851, and JP22H05280. This work was also supported by the TAKEUCHI Foundation (Grant Number 2021-J-17).

Data Availability Statement: All data generated or analyzed during this study are available within the article.

Acknowledgments: This work was performed under the Joint Usage/Research Center on Joining and Welding, Osaka University.

Conflicts of Interest: The authors declare no conflict of interest.

References

1. Yaoita, S.; Watanabe, T.; Sasaki, T. Brazing of Cemented Carbides at Lower Temperatures. *Adv. Mater. Res.* **2011**, *409*, 865–870. [CrossRef]
2. Wu, X.; Li, L.; He, N.; Zhao, G.; Shen, J. Experimental Investigation on Direct Micro Milling of Cemented Carbide. *Micromachines* **2019**, *10*, 147. [CrossRef] [PubMed]
3. Algarni, M. Mechanical Properties and Microstructure Characterization of AISI 'D2' and 'O1' Cold Work Tool Steels. *Metals* **2019**, *9*, 1169. [CrossRef]
4. Yamashita, Y.; Funada, Y.; Kunimine, T.; Sato, Y.; Tsukamoto, M. Formation of cemented tungsten carbide layer with compositional gradient processed by directed energy deposition. *Mater. Sci. Forum* **2021**, *1016*, 1676–1681. [CrossRef]
5. Wanjara, P.; Backman, D.; Sikan, F.; Gholipour, J.; Amos, R.; Patnaik, P.; Brochu, M. Microstructure and Mechanical Properties of Ti-6Al-4V Additively Manufactured by Electron Beam Melting with 3D Part Nesting and Powder Reuse Influences. *J. Manuf. Mater. Process.* **2022**, *6*, 21. [CrossRef]
6. Zhang, L.C.; Chen, L.Y.; Zhou, S.; Luo, Z. Powder bed fusion manufacturing of beta-type titanium alloys for biomedical implant applications: A review. *J. Alloys Compd.* **2023**, *936*, 168099. [CrossRef]
7. Calignano, F.; Galati, M.; Iuliano, L. A Metal Powder Bed Fusion Process in Industry:Qualification Considerations. *Machines* **2019**, *7*, 72. [CrossRef]
8. Kotadia, H.R.; Gibbons, G.; Das, A.; Howes, P.D. A review of Laser Powder Bed Fusion Additive Manufacturing of aluminium alloys: Microstructure and properties. *Addit. Manuf.* **2021**, *46*, 102155. [CrossRef]
9. Silbernagel, C.; Gargalis, L.; Ashcroft, I.; Hague, R.; Galea, M.; Dickens, P. Electrical resistivity of pure copper processed by medium-powered laser powder bed fusion additive manufacturing for use in electromagnetic applications. *Addit. Manuf.* **2019**, *29*, 100831. [CrossRef]

10. Qi, H.; Mazumder, J.; Ki, H. Numerical Simulation of Heat Transfer and Fluid Flow in Coaxial Laser Cladding Process for Direct Metal Deposition. *J. Appl. Phys.* **2006**, *33*, 101175. [CrossRef]
11. Pereira, J.C.; Aguilar, D.; Tellería, I.; Gómez, R.; Sebastian, M.S. Semi-Continuous Functionally Graded Material Austenitic to Super Duplex Stainless Steel Obtained by Laser-Based Directed Energy Deposition. *J. Manuf. Mater. Process.* **2023**, *7*, 150. [CrossRef]
12. Shishkovsky, I.; Kakovkina, N.; Nosova, E.; Khaimovich, A. Laser In Situ Synthesis of Gradient Fe-Ti Composite during Direct Energy Deposition Process. *J. Manuf. Mater. Process.* **2023**, *7*, 66. [CrossRef]
13. Sato, Y.; Tsukamoto, M.; Shobu, T.; Funada, Y.; Yamashita, Y.; Hara, T.; Sengoku, M.; Sakon, Y.; Ohkubo, T.; Yoshida, M.; et al. In situ X-ray observations of pure-copper layer formation with blue direct diode lasers. *Appl. Surf. Sci.* **2019**, *480*, 861–867. [CrossRef]
14. Saboori, A.; Aversa, A.; Marchese, G.; Biamino, S.; Lombardi, M.; Fino, P. Application of Directed Energy Deposition-Based Additive Manufacturing in Repair. *Appl. Sci.* **2019**, *9*, 3316. [CrossRef]
15. Kunimine, T.; Miyazaki, R.; Yamashita, Y.; Funada, Y. Effects of Laser-Beam Defocus on Microstructural Features of Compositionally Graded WC/Co-Alloy Composites Additively Manufactured by Multi-Beam Laser Directed Energy Deposition. *Sci. Rep.* **2020**, *10*, 1–11. [CrossRef] [PubMed]
16. Adachi, S.; Yamaguchi, T.; Ueda, N. Formation and Properties of Nitrocarburizing S-Phase on AISI 316L Stainless Steel-Based WC Composite Layers by Low-Temperature Plasma Nitriding. *Metals* **2021**, *11*, 1538. [CrossRef]
17. Ranjan, R.; Das, A.K. Improving the Resistance to Wear and Mechanical Characteristics of Cladding Layers on Titanium and Its Alloys: A Review. *Tribol. Ind.* **2023**, *45*, 136–152. [CrossRef]
18. Yamashita, Y.; Nakamura, M.; Sakai, M.; Kunimine, T.; Sato, Y.; Funada, Y.; Tsukamoto, M. In Situ Evaluation of Crack Generation Using Acoustic Emission Technique during Laser Cladding of WC-Co Cemented Carbide via Multi-Beam Laser Metal Deposition. *Mater. Sci. Forum* **2023**, *1083*, 153–158. [CrossRef]
19. Brückner, F.; Lepski, D.; Beyer, E. Modeling the Influence of Process Parameters and Additional Heat Sources on Residual Stresses in Laser Cladding. *J. Therm. Spray Technol.* **2007**, *16*, 355–373. [CrossRef]
20. Shi, Y.; Zhou, X.; Wang, X.; Feng, X.; Peng, L. Effects of Electromagnetic Fields on the Microstructure of Laser Cladding. *Materials* **2022**, *15*, 4198. [CrossRef]
21. Itagaki, H.; Yachi, T.; Ogiso, H.; Sato, H.; Yamashita, Y.; Yasuoka, J.; Funada, Y. DC Arc Plasma Treatment for Defect Reduction in WC-Co Granulated Powder. *Metals* **2020**, *10*, 975. [CrossRef]
22. Mazzarisi, M.; Campanelli, S.L.; Angelastro, A.; Palano, F.; Dassisti, M. In situ monitoring of direct laser metal deposition of a nickel-based superalloy using infrared thermography. *J. Adv. Manuf. Technol.* **2021**, *112*, 157–173. [CrossRef]
23. Funada, Y.; Yamashita, Y.; Sakon, Y.; Tsukamoto, M. Development and Bead Formation Properties of Multiple Laser Coating Technology with Centered Powder Feeding. *J. Smart Process.* **2019**, *8*, 19–24. [CrossRef]
24. Samsonov, G.V.; Vinitskii, I.M. *Handbook of Refractory Compounds*; IFI/Plenum Data Company: New York, NY, USA, 1980.
25. Greenwood, N.N.; Earnshaw, A. *Chemistry of the Elements*, 2nd ed.; Butterworth-Heinemann: Oxford, UK, 1997.
26. Buch, A. Pure Metals Properties. In *A Scientific-Technical Handbook*, 1st ed.; ASM International and Freund Publishing House Ltd.: Materials Park, OH, USA, 1999.
27. RiuNet UPV. Available online: https://riunet.upv.es/bitstream/handle/10251/113733/ANEXO_15329653939736146149195128546168.pdf?isAllowed=y&sequence=2 (accessed on 31 July 2023).
28. Ochiai, H.; Ukai, T. Weld Residual Stress Analysis of WC-Ni Cemented Carbide Using Thermo-Elastoplasticity. *J. Jpn. Soc. Des. Eng.* **2005**, *40*, 410–415.
29. Gietzelt, T.; Eichhorn, L. *Mechanical Micromachining by Drilling, Milling and Slotting*; Kahrizi, M., Ed.; IntechOpen: Rijeka, Croatia, 2012; pp. 159–183.
30. Kruth, J.P.; Wang, X.; Laoui, T.; Froyen, L. Lasers and materials in selective laser sintering. *Assem. Autom.* **2003**, *23*, 357–371. [CrossRef]
31. Weber, M.J.; Dotsenko, A.V.; Glebov, L.B.; Tsekhomsky, V.A. *Handbook of Optical Materials*; CRC Press LCC: Washington, DC, USA, 2002; Volume 40.
32. Yang, Y.; Zhang, C.; Wang, D.; Nie, L.; Wellmann, D.; Tian, Y. Additive manufacturing of WC-Co hardmetals: A review. *Int. J. Adv. Manuf. Technol.* **2020**, *108*, 1653–1673. [CrossRef]